1 Study Area

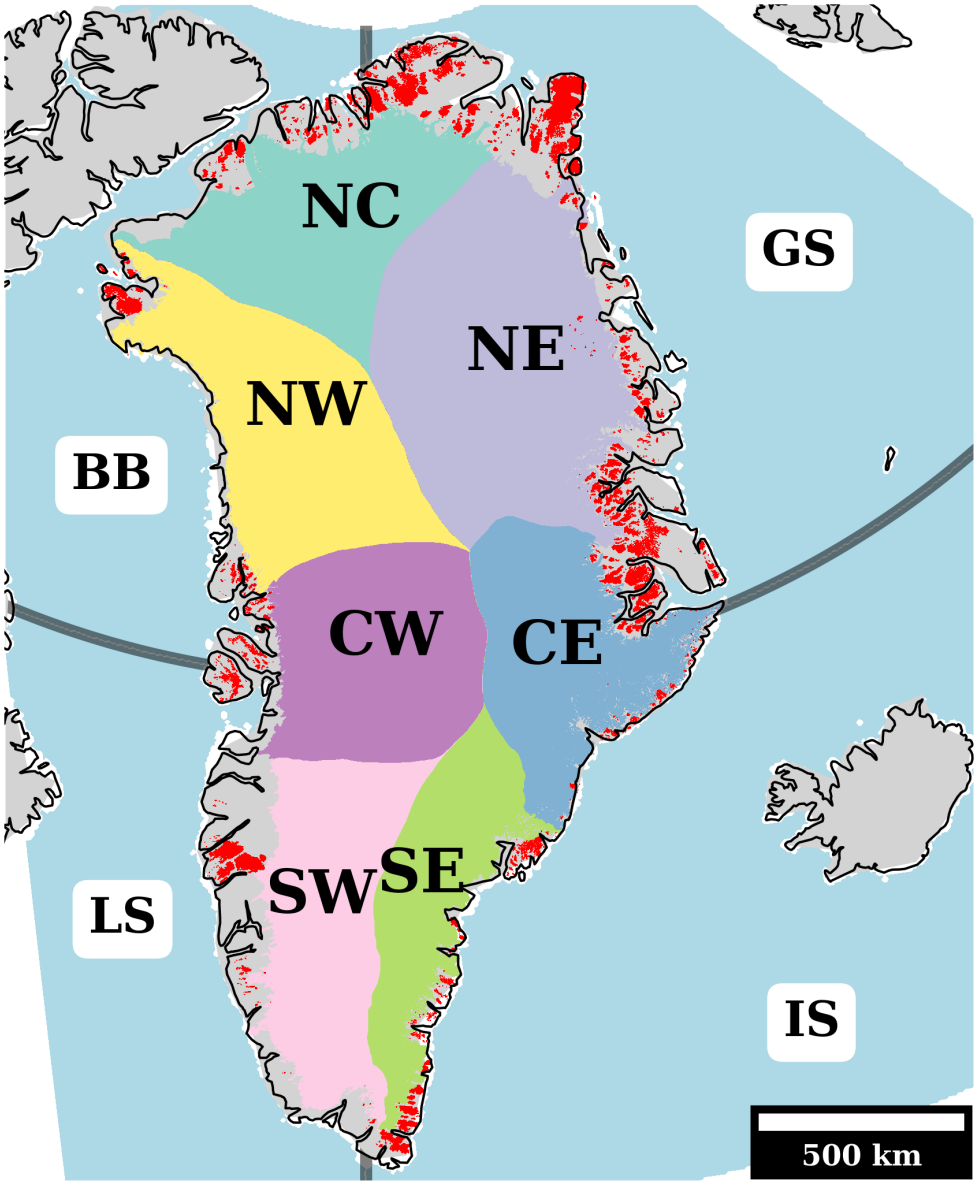

Figure S1. Map of the Greenland ice sheet and peripheral glaciers (in red) separated by main drainage basins. The meridian 45°W and the parallel 70°N are used to divide the adjacent seas (in blue) in four quadrants: Baffin Bay (BB); Labrador Sea (LB); Greenland Sea (GS); and Irminger/Icelandic Sea (IS). The Denmark Strait is situated in between Greenland and Iceland.

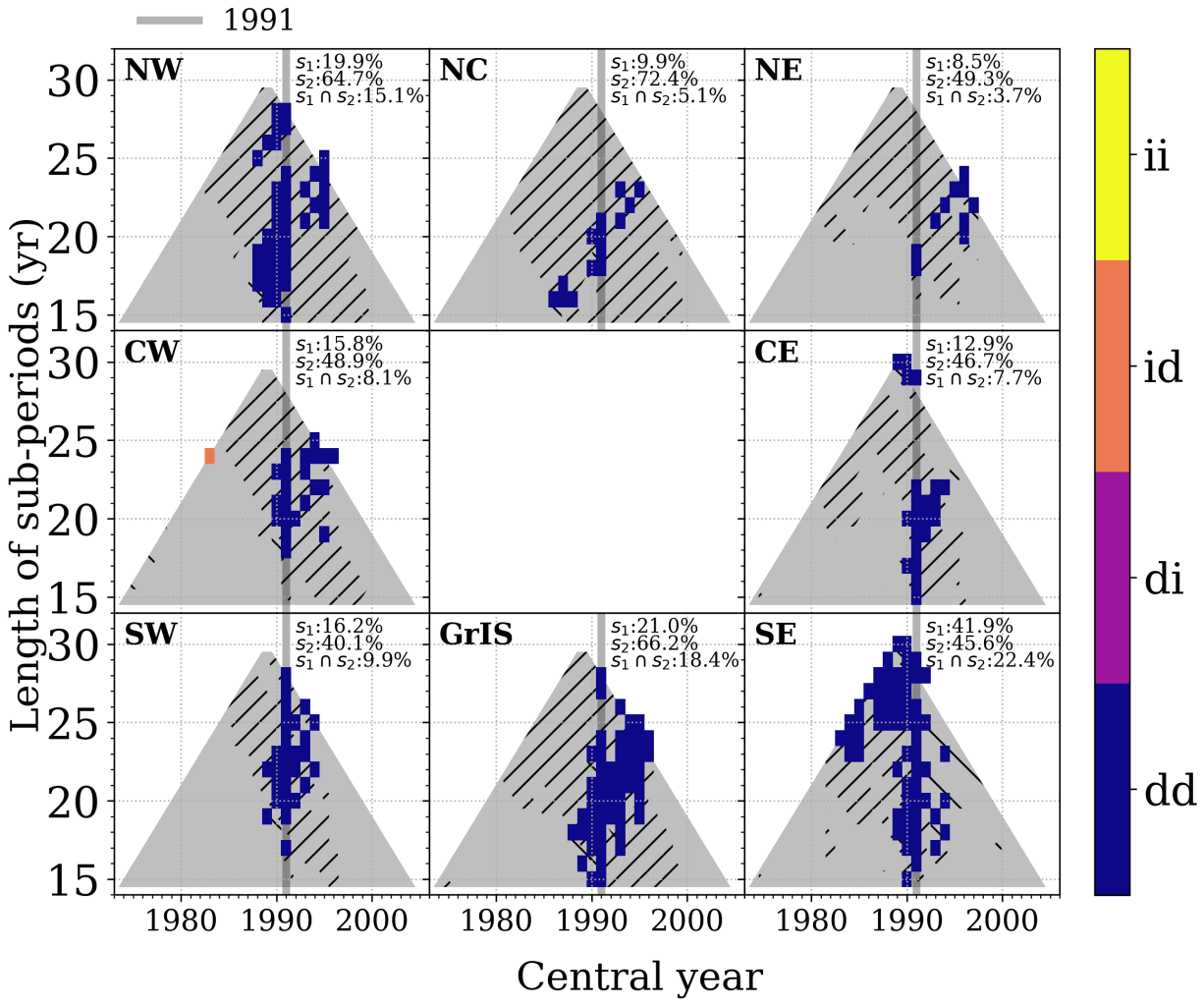

Figure S2. Regional Mann-Kendall (M-K) trend classification by splitting the data-set in two equally-sized sub-periods (y-axis) and varying its time-center (x-axis) for the surface integrated ablation rate in summer from RACMO2 between 1959-2020. Regional M-K trend classification is only shown when both sub-periods show confidence higher than 90%. i(d) stands for increasing(decreasing) trend prior to and subsequent to the central (splitting) year. Significant first (second) sub-period trends are left (right) tilted, whereas the rest is illustrated by the gray shaded area. The upper-right corner indicates the relative frequency of significant sub-periods. For reference, 1991 is marked with a thick line.

Since the late-1980s, the (sub-)period length increases for recent central splitting years in most regions, which indicates high surface mass loss variability among short sub-periods. Moreover, significant surface mass loss trends are more common in recent decades, ranging from 40% in the southwest to 72% (out of all possible sub-period trends - gray shaded area) in north Greenland. Southeast is the region with more significant trends among periods. Except in the northern part and the northeast, most significant trends are found for the central splitting year of 1990-91 in a wide range of period's lengths and with the highest ratios. Moreover, the performed trend analysis suggests no influence from the Pinatubo eruption in 1992.

3 Climate oscillations

3.1 Clustering Analysis

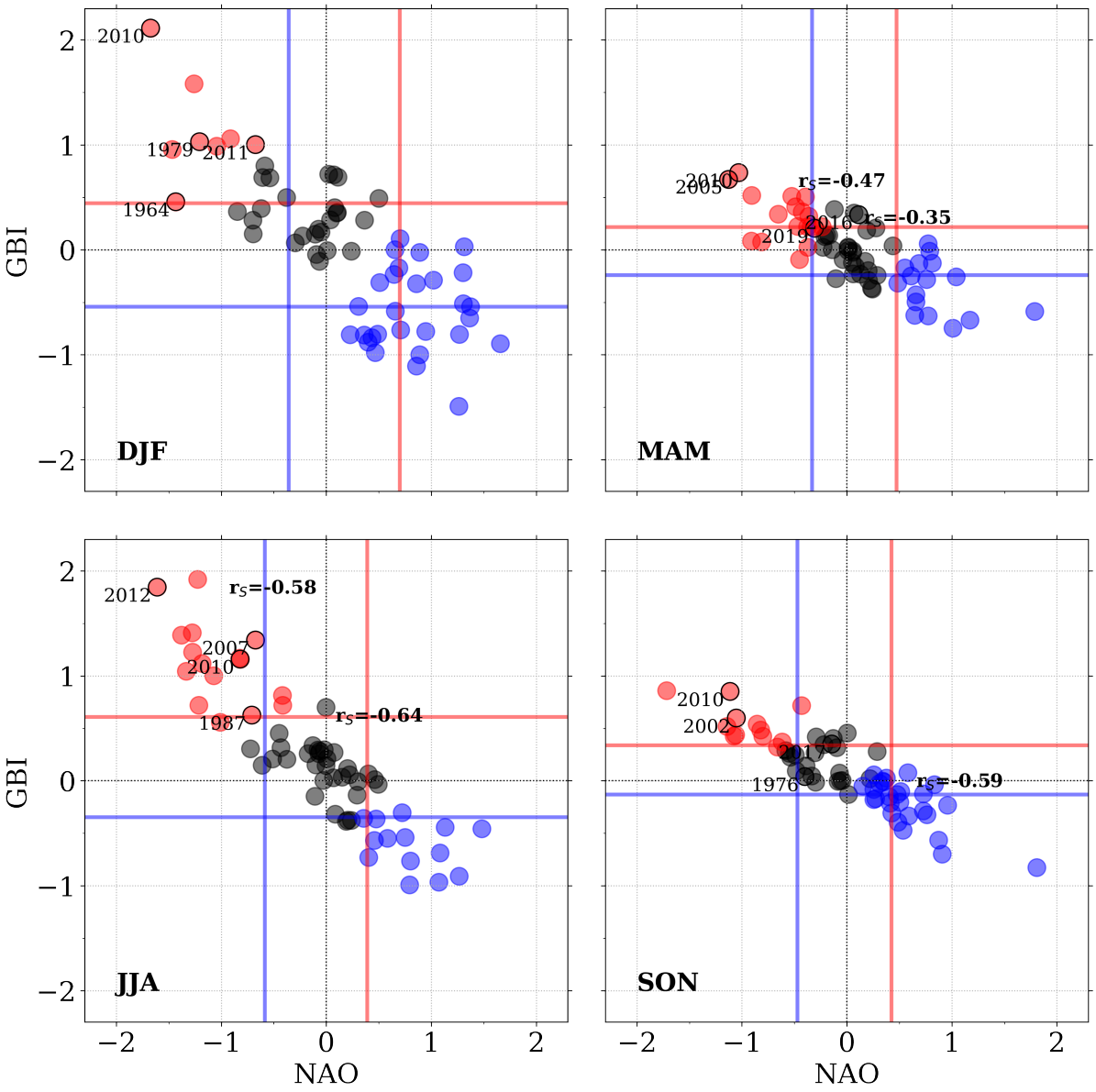

Figure S3. Seasonal NAO vs GBI phase and corresponding clusters: positive (red); neutral (black); and negative (blue) phase. The seasonal 25^{th} (blue) and 75^{th} (red) percentile are also shown as lines. The Spearman correlation coefficient (r_S) is shown for clusters with significance higher than 90%. Years whose seasonal GrIS IWV overcomes the 95^{th} percentile are shown and indicated with a dark circle.

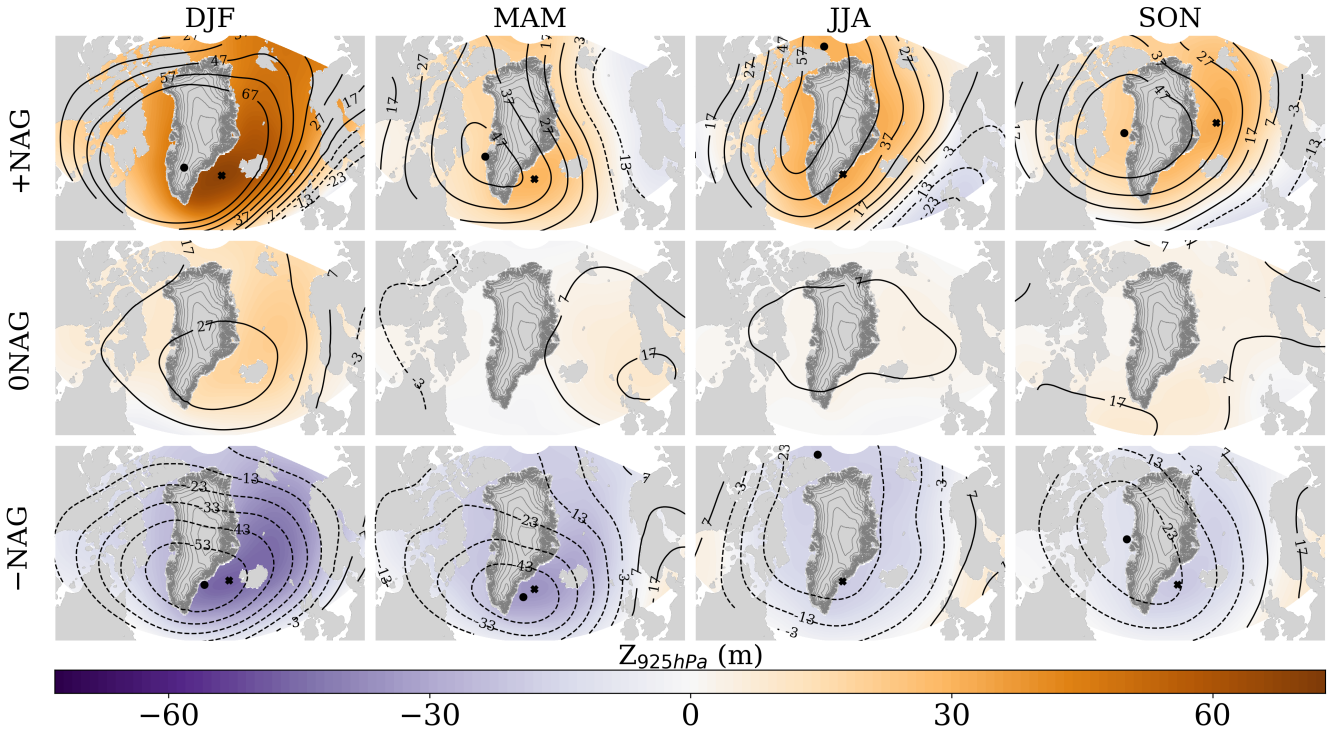

Figure S4. Inter-seasonal 500 hPa geopotential height anomaly (contour lines; positive: solid and negative:dashed; spaced in 10 m intervals), and 925 hPa geopotential height anomaly for each NAG phase with respect to climatology (1959-2000). The ridge (trough) at 925 and 500-hPa geopotential height anomaly is indicated as dot and cross, respectively, for +NAG(−NAG).

Figure S5 shows the seasonal and spatial integrated surface mass balance according to subsection 2.2, NAG-colored balance (in bars), and the 1991-2020 surface ablation regression.

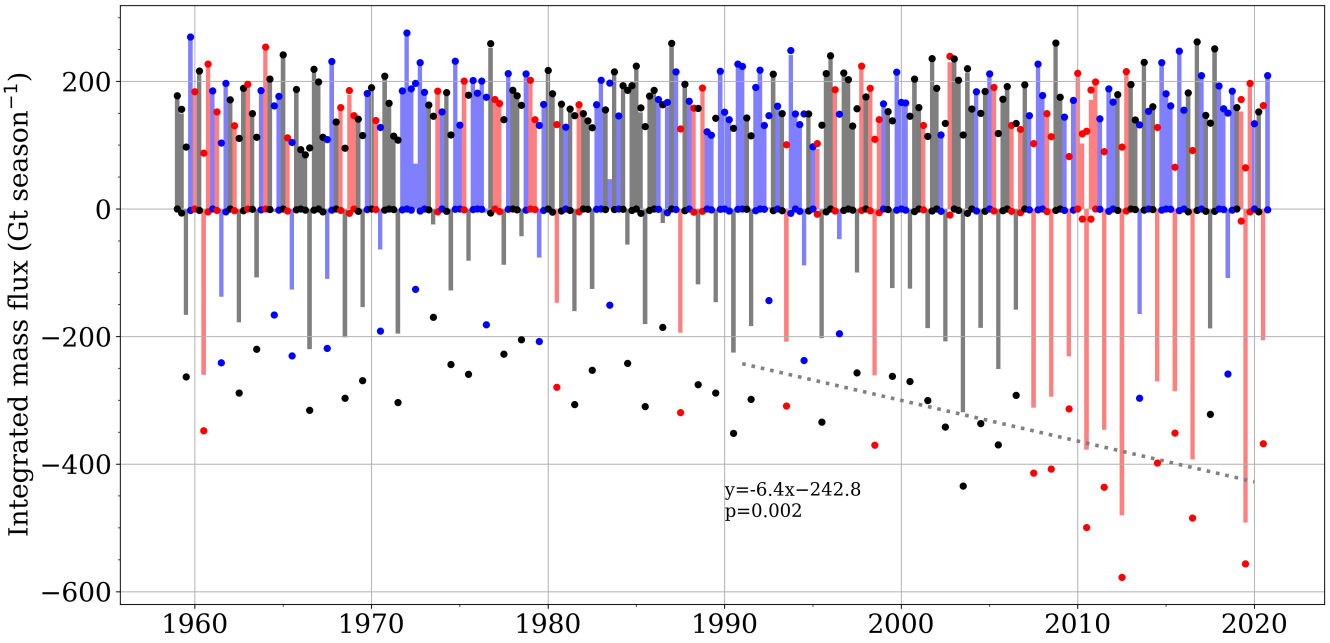

Figure S5. The NAG seasonal and regionally integrated surface mass flux over the GrIS from 1959 until 2020 from RACMO2. North Atlantic influence on Greenland (NAG) is color-coded according to its phase (positive: red; negative: blue; neutral: black). Bubbles (also color-coded based on NAG phase) correspond to seasonal ablation (accumulation) mass flux. Bars (also NAG color-coded) indicate the seasonal surface mass balance. The dotted line is the regression line for summer ablation using T-S slope and the K-T interception between 1991 and 2020 with the associated slope p-value (by the M-K trend test).

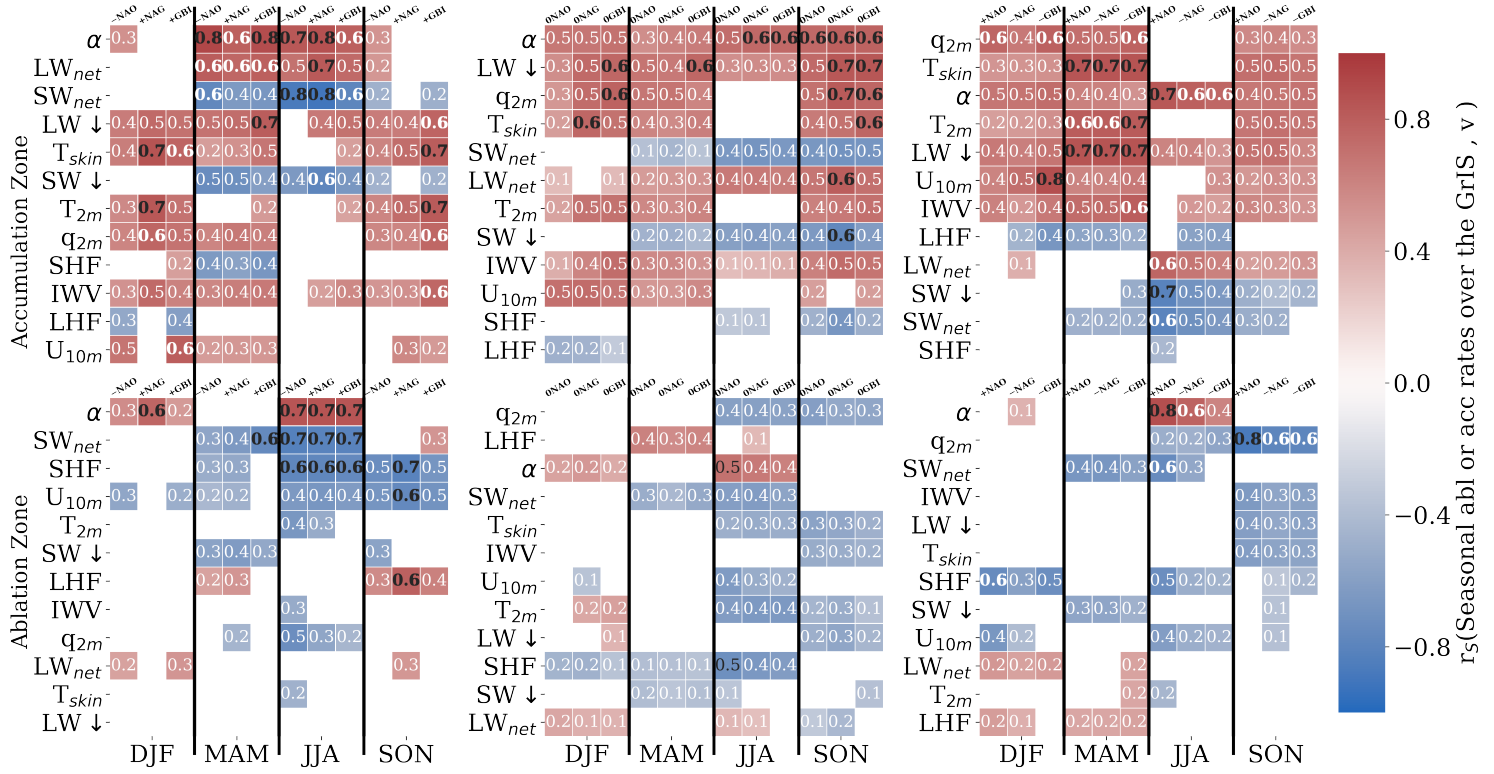

Figure S6. Seasonal correlation matrices between seasonal accumulation (or ablation) rates and atmospheric variables from RACMO2 contributing to the SEB depending on NAO, NAG and GBI phases between 1959 and 2020. The Spearman correlation coefficient is color-coded and the determination coefficient is noted. Correlation matrices are sorted from overall large determination coefficient to small determination coefficient, and highlighted when $r_S^2 \geq 0.6$

4 Additional inter-seasonal NAG climatology

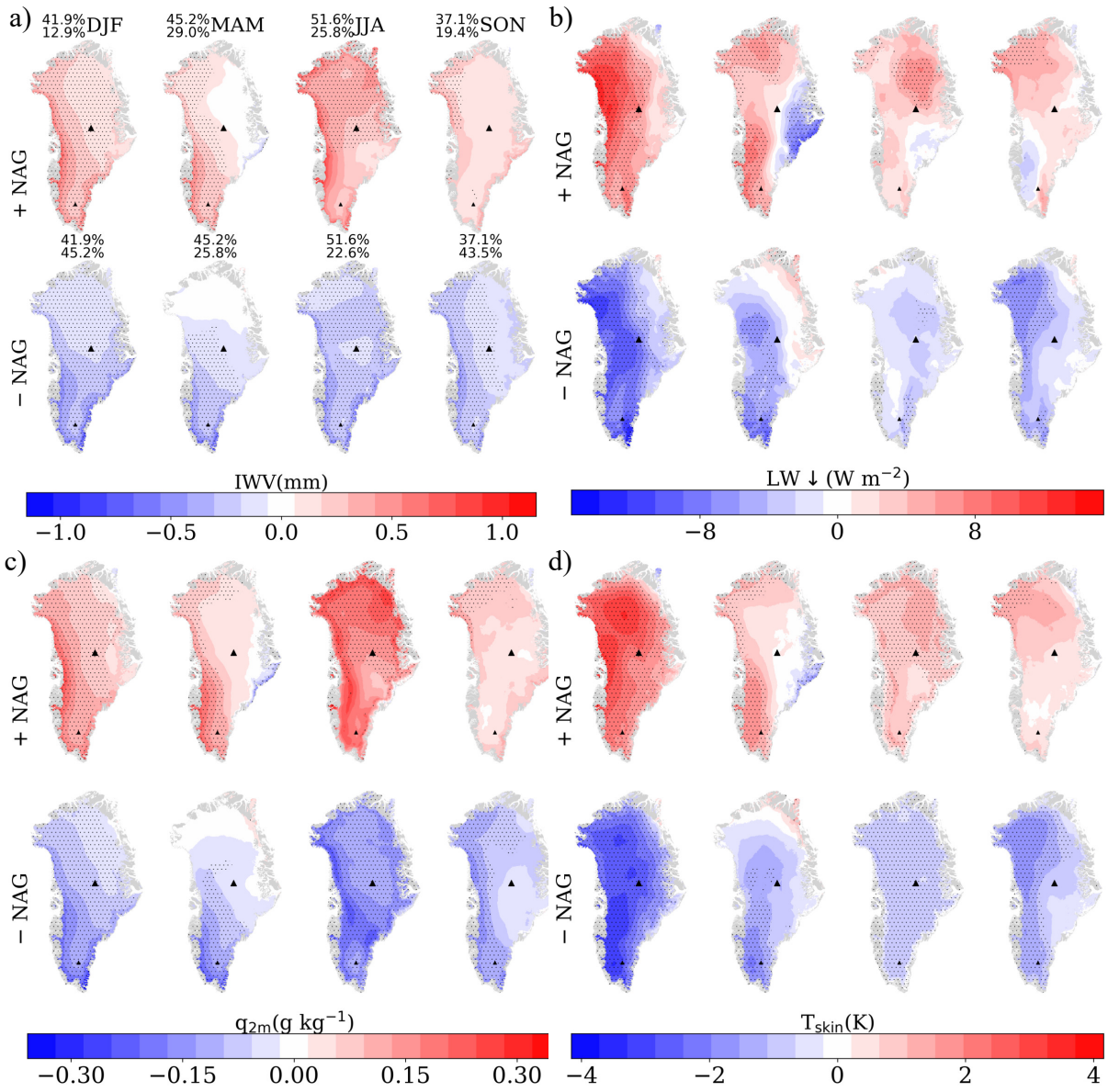

Figure S7. Seasonal and spatial anomalies for (a) integrated water vapor, (b) incoming long-wave radiation, (c) near-surface specific humidity and (d) skin temperature between opposite North Atlantic influence on Greenland (NAG) phases wrt. the neutral phase ($\overline{+(-)\text{NAG}}$ - $\overline{0\text{NAG}}$) for RACMO2 between 1959 and 2020. At the upper left (right) side of each subtitle is indicated the number of neutral (positive or negative, depending on the row) NAG phases in each season to produce $\overline{(+/0/-)\text{NAG}}$ composites. For reference, Summit and South Dome are marked with big and small black triangles, respectively. Stippled regions indicate significant areas (based on the Wilcoxon rank-sum statistic test for unpaired sets) with a confidence higher than 90%.

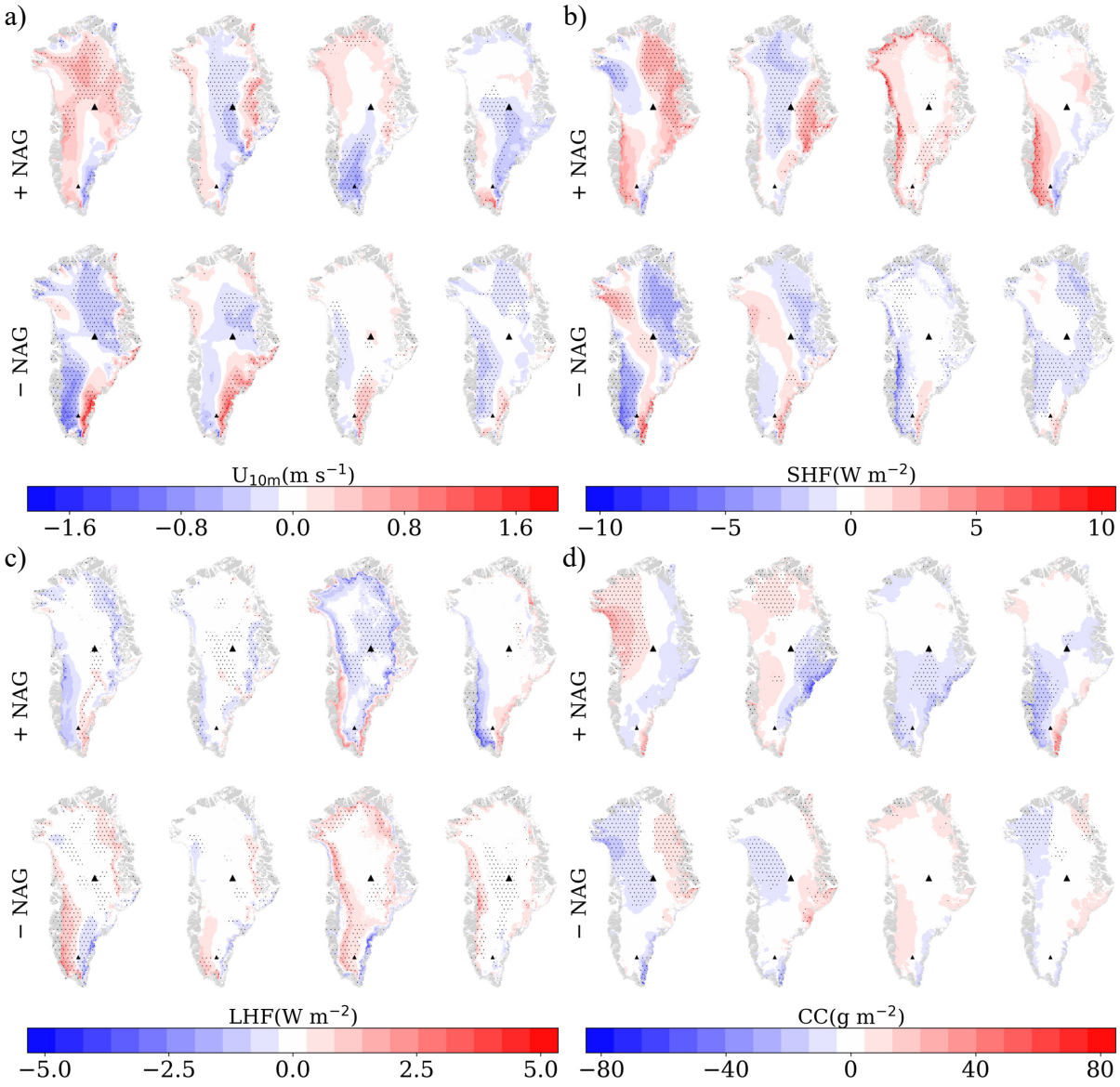

Figure S8. Seasonal and spatial anomalies for (a) near-surface wind speed, (b) sensible heat flux, (c) latent heat flux and (d) cloud content between opposite North Atlantic influence on Greenland (NAG) phases wrt. the neutral phase ($\overline{+(-)\text{NAG}}$ - $\overline{0\text{NAG}}$) for RACMO2 between 1959 and 2020. At the upper left (right) side of each subtitle is indicated the number of neutral (positive or negative, depending on the row) NAG phases in each season to produce $\overline{(+/0/-)\text{NAG}}$ composites. For reference, Summit and South Dome are marked with big and small black triangles, respectively. Stippled regions indicate significant areas (based on the Wilcoxon rank-sum statistic test for unpaired sets) with a confidence higher than 90%.

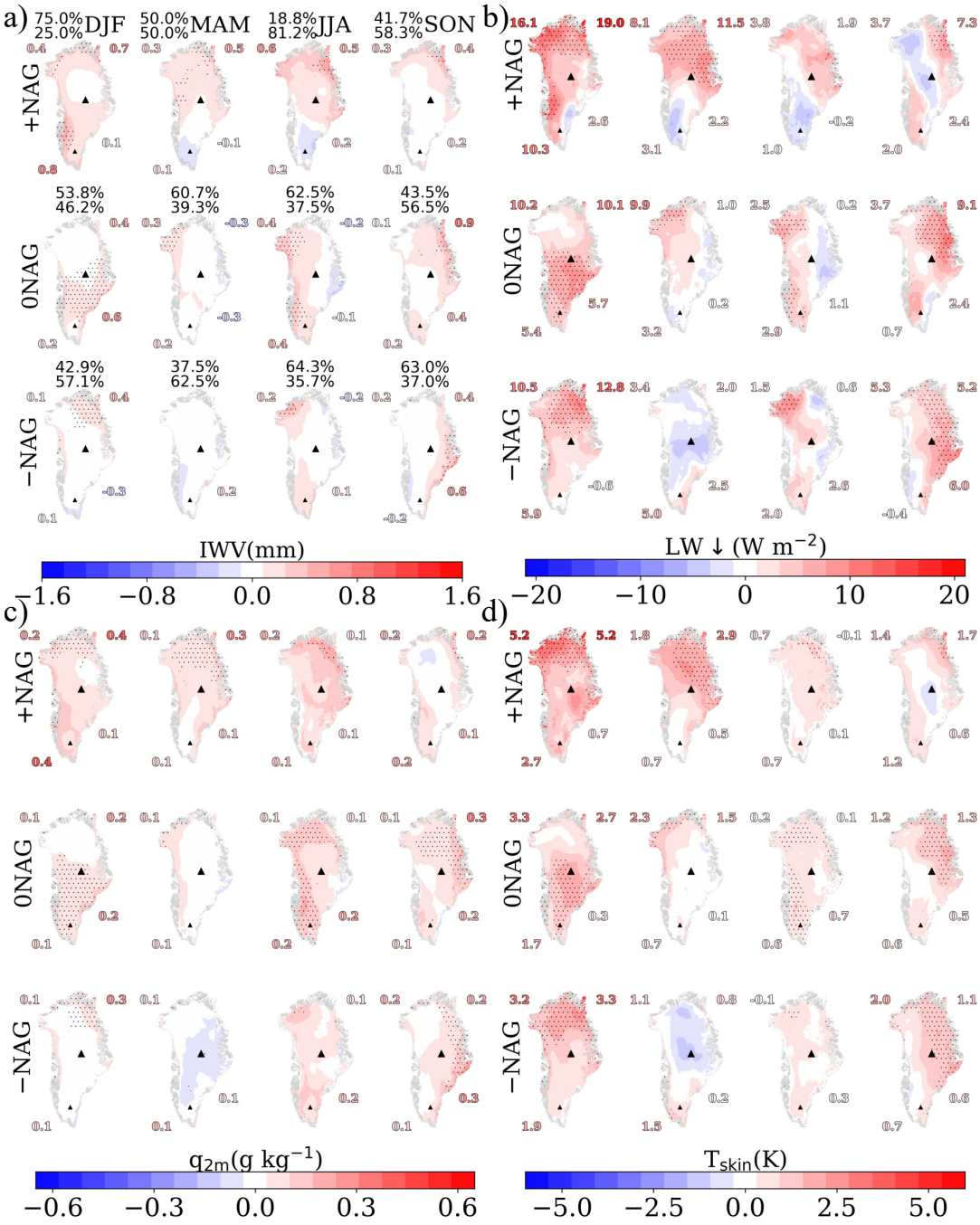

Figure S9. Seasonal and spatial differences between the second (1991-2020) and the first (1959-1990) sub-period composite for (a) integrated water vapor, (b) incoming long-wave, (c) near-surface specific humidity, and (d) skin temperature as dependent on the GBI phase. On the left side of the first panel is indicated the frequency of each GBI phase before (upper #%) and (lower #%) 1991. For reference, Summit and South Dome are marked as big and small triangles, respectively. Stippled regions indicate significant areas (based on the Wilcoxon rank-sum statistic test for two unpaired sets) with a confidence higher than 90%. Differences between composites over the adjacent seas are also shown (Baffin Bay: upper left; Greenland Sea: upper right; Irminger Sea (lower right) and Labrador Sea (lower left).

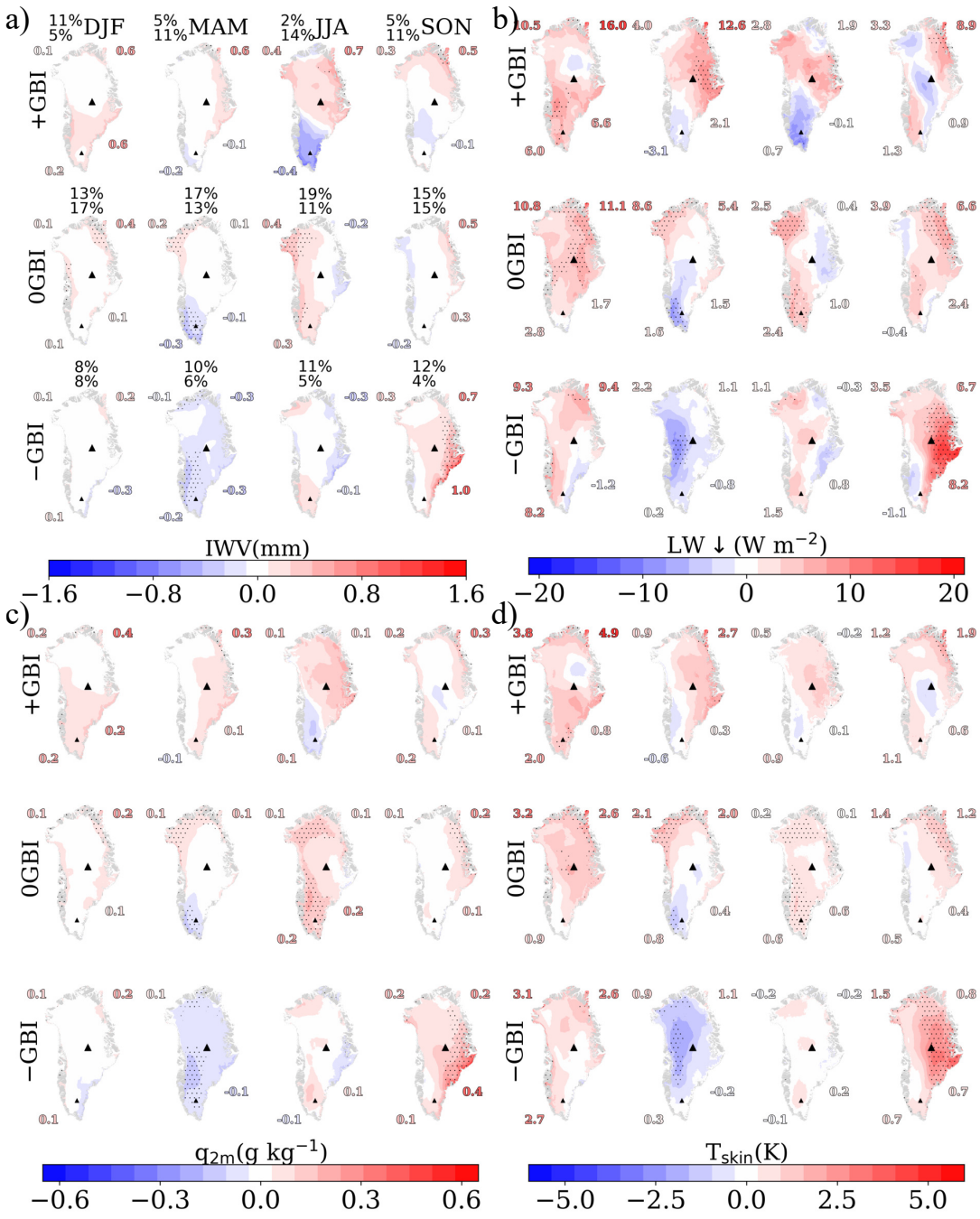

Figure S10. Seasonal and spatial differences between the second (1991-2020) and the first (1959-1990) sub-period composite for integrated water vapor (a), incoming long-wave (b), near-surface specific humidity (c), and skin temperature (d) depending on the GBI phase. On the left side of the first panel is indicated the frequency of each GBI phase before (upper #%) and (lower #%) 1991. For reference, Summit and South Dome are marked as big and small triangles, respectively. Stippled regions indicate significant areas (based on the Wilcoxon rank-sum statistic test for two unpaired sets) with a confidence higher than 90%. Differences between composites over the adjacent seas are also shown (Baffin Bay: upper left; Greenland Sea: upper right; Irminger Sea (lower right) and Labrador Sea (lower left).

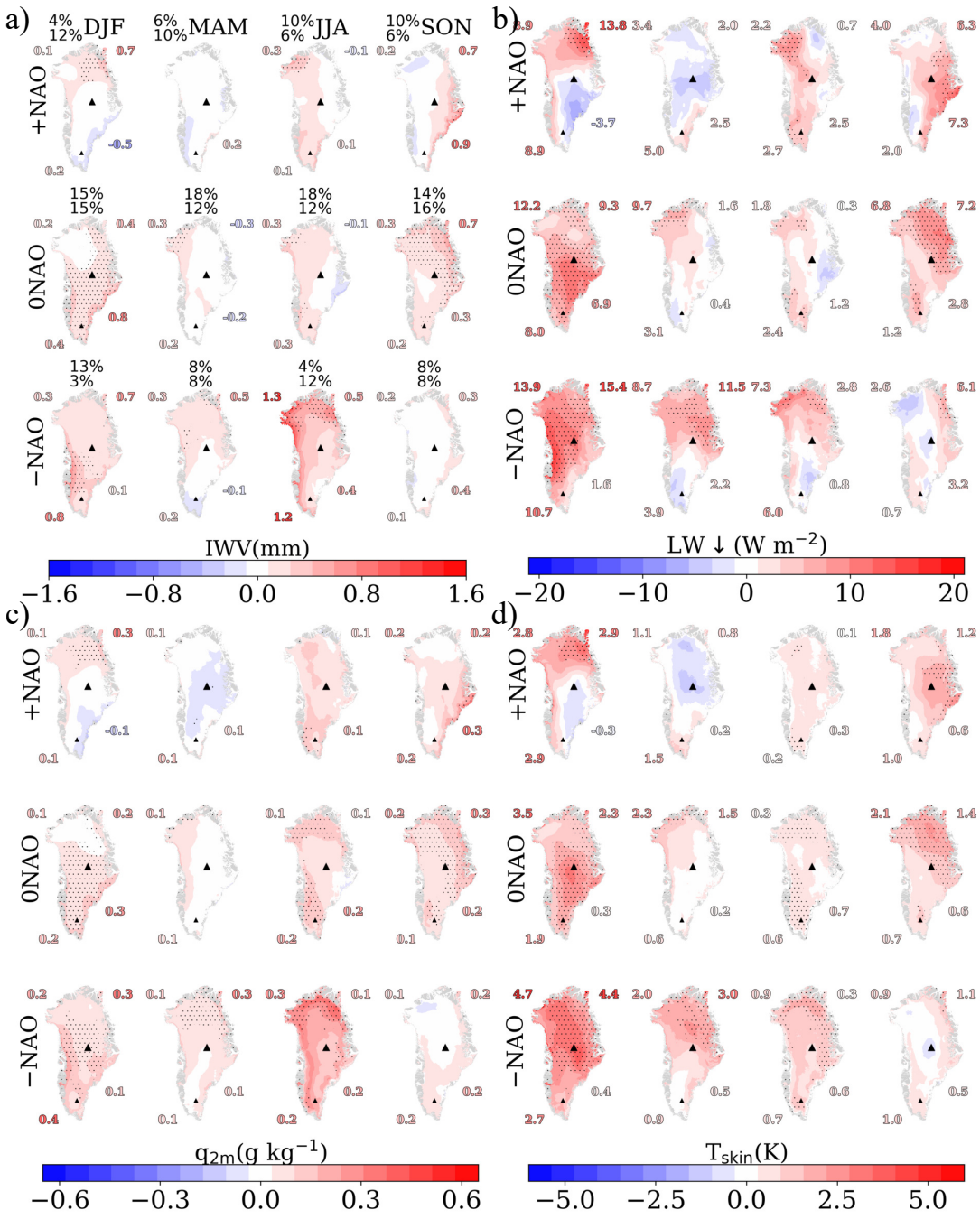

Figure S11. Seasonal and spatial differences between the second (1991-2020) and the first (1959-1990) sub-period composite for integrated water vapor (a), incoming long-wave (b), near-surface specific humidity (c), and skin temperature (d) depending on the NAO phase. On the left side of the first panel is indicated the frequency of each GBI phase before (upper #%) and (lower #%) 1991. For reference, Summit and South Dome are marked as big and small triangles, respectively. Stippled regions indicate significant areas (based on the Wilcoxon rank-sum statistic test for two unpaired sets) with a confidence higher than 90%. Differences between composites over the adjacent seas are also shown (Baffin Bay: upper left; Greenland Sea: upper right; Irminger Sea (lower right) and Labrador Sea (lower left).

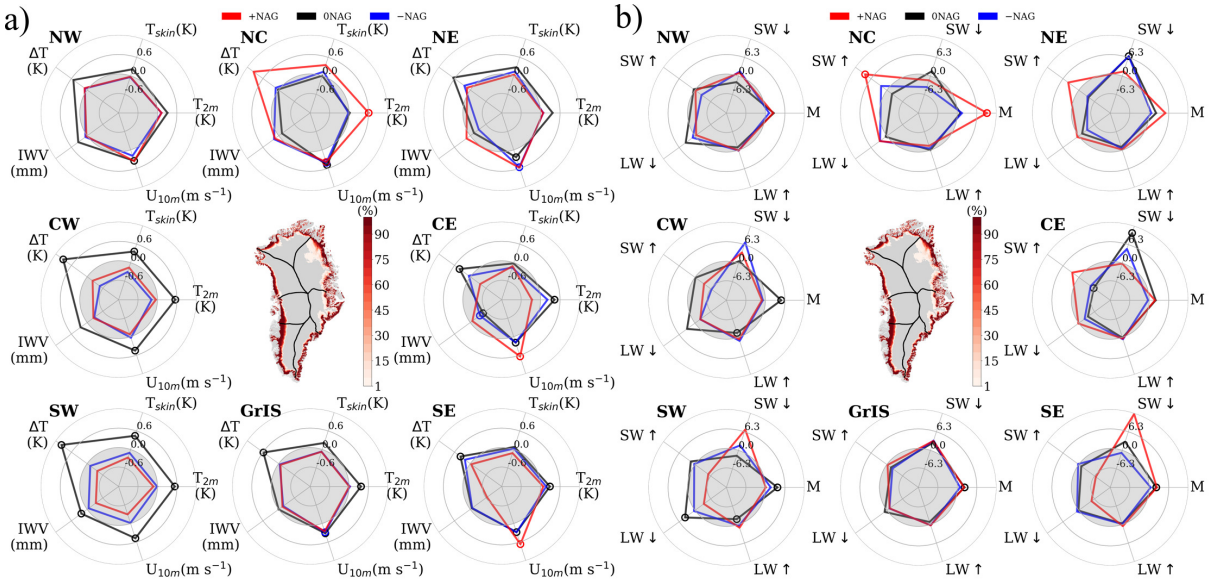

Figure S12. Changes in atmospheric variables influencing SEB components in the summer ablation zone for each NAG phase. The spatial relative frequency of accumulation is shown at the center. Negative changes are limited by the gray area. Hollow circles indicate significant mean differences based on the Wilcoxon rank-sum statistic test for unpaired sets with a confidence higher than 90%.

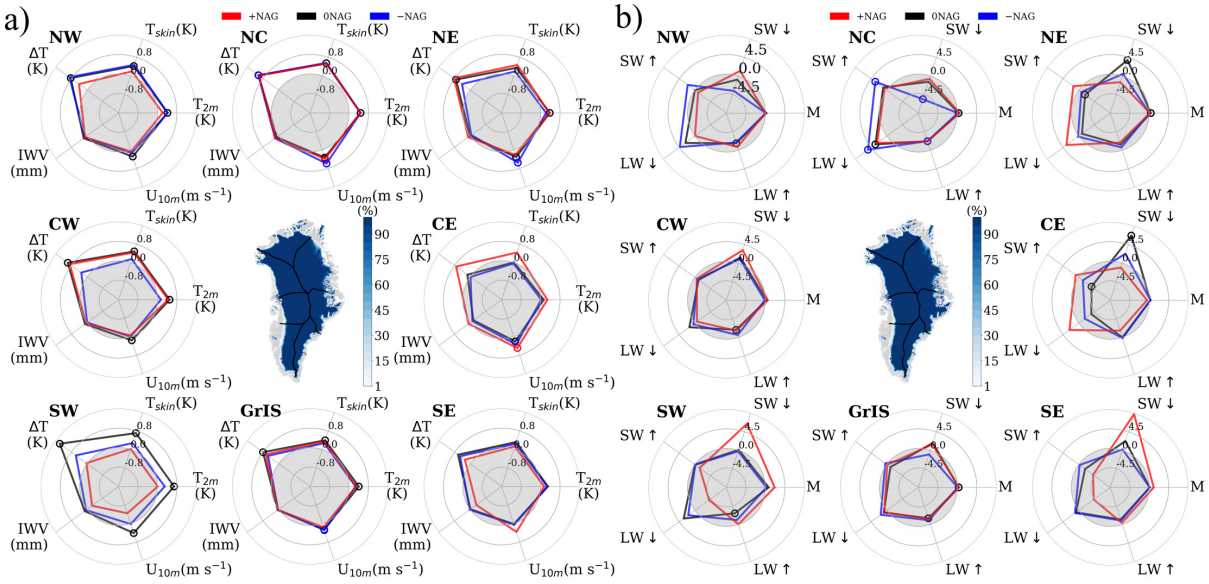

Figure S13. Changes in atmospheric variables influencing SEB components in the summer accumulation zone for each NAG phase. The spatial relative frequency of accumulation is shown at the center. Negative changes are limited by the gray area. Hollow circles indicate significant mean differences based on the Wilcoxon rank-sum statistic test for unpaired sets with a confidence higher than 90%.

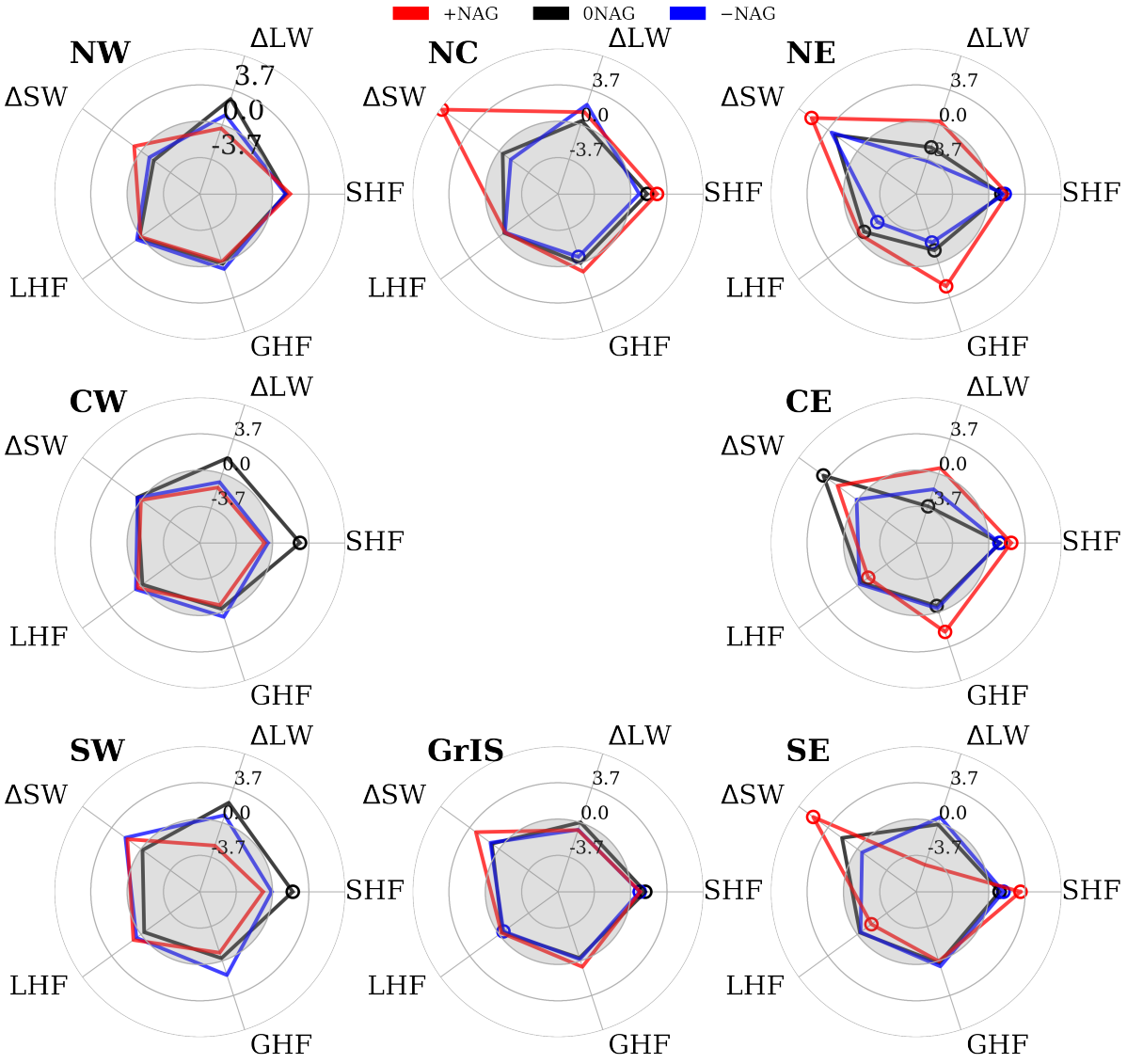

Figure S14. Changes in atmospheric variables influencing SEB components in the summer ablation zone for each NAG phase. The spatial relative frequency of accumulation is shown at the center. Negative changes are limited by the gray area. Hollow circles indicate significant mean differences based on the Wilcoxon rank-sum statistic test for unpaired sets with a confidence higher than 90%.

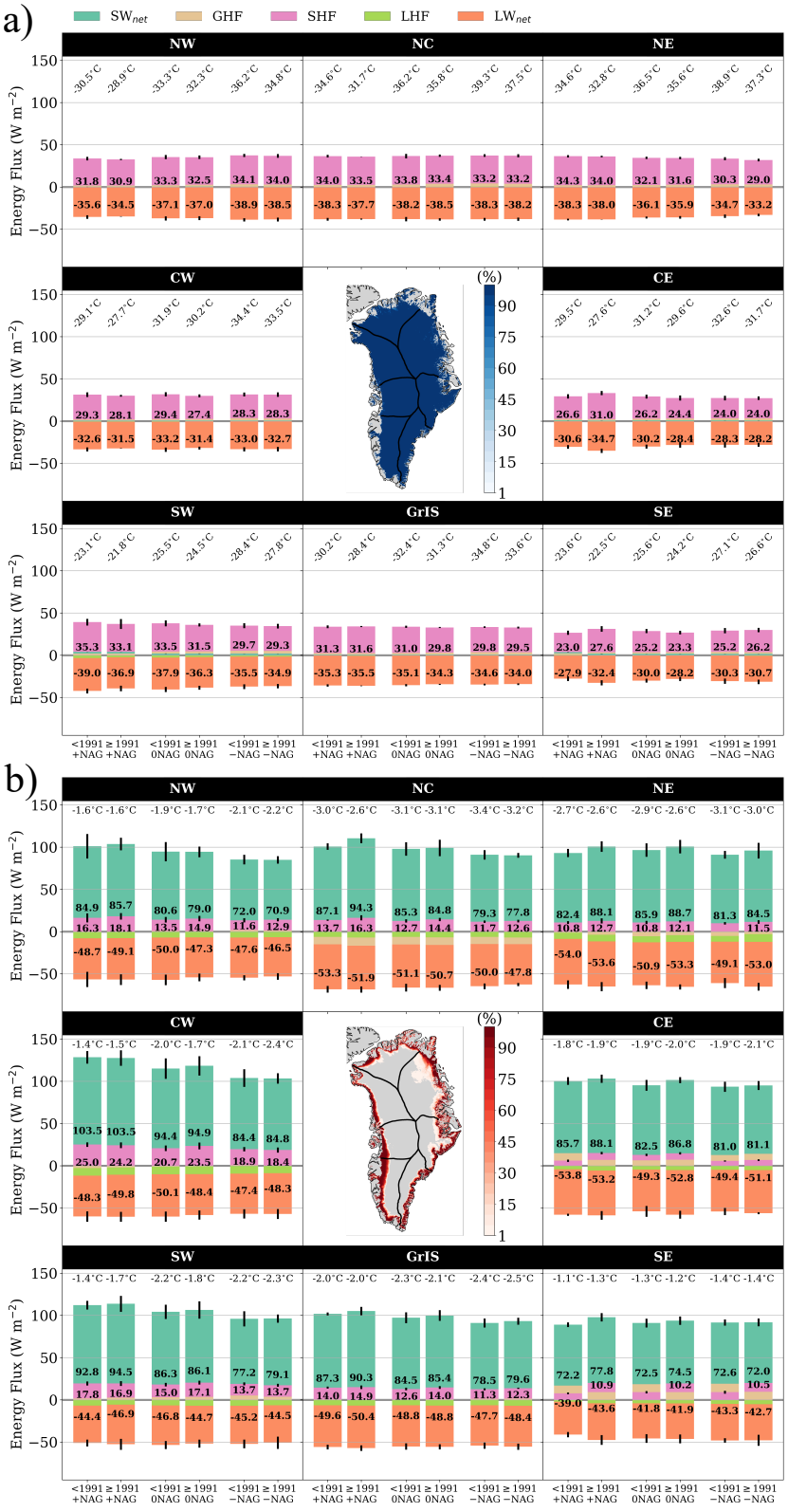

Figure S15. Regional surface energy fluxes before 1991 (<1991) and after (≥1991) in the winter accumulation zone (a) and summer ablation zone for each NAG phase. Areal accumulation (a) and ablation (b) zone contributing to regional averages is shown at the center as relative frequencies.

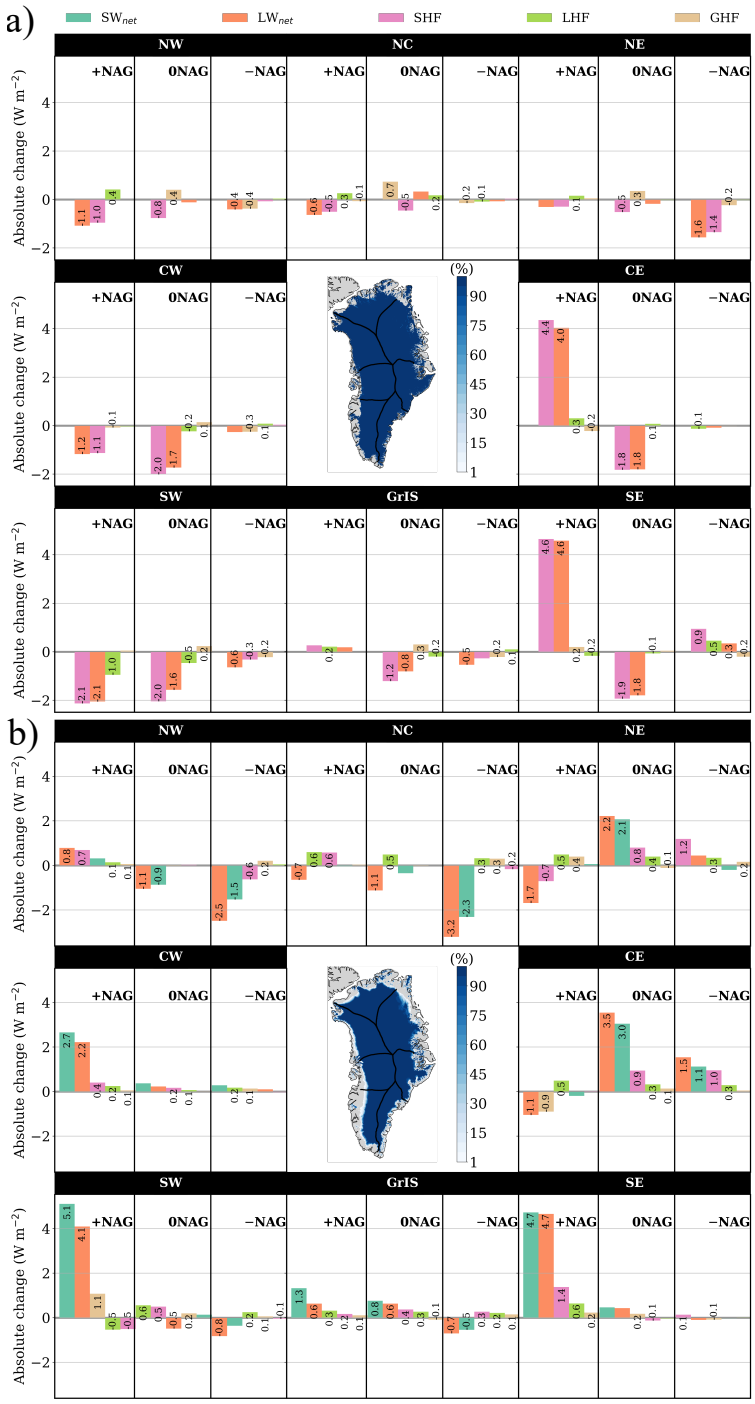

Figure S16. Changes in surface energy fluxes in the winter (a) and summer (b) accumulation zone for each NAG phase. Areal accumulation zone contributing to regional averages is shown at the center as relative frequencies.

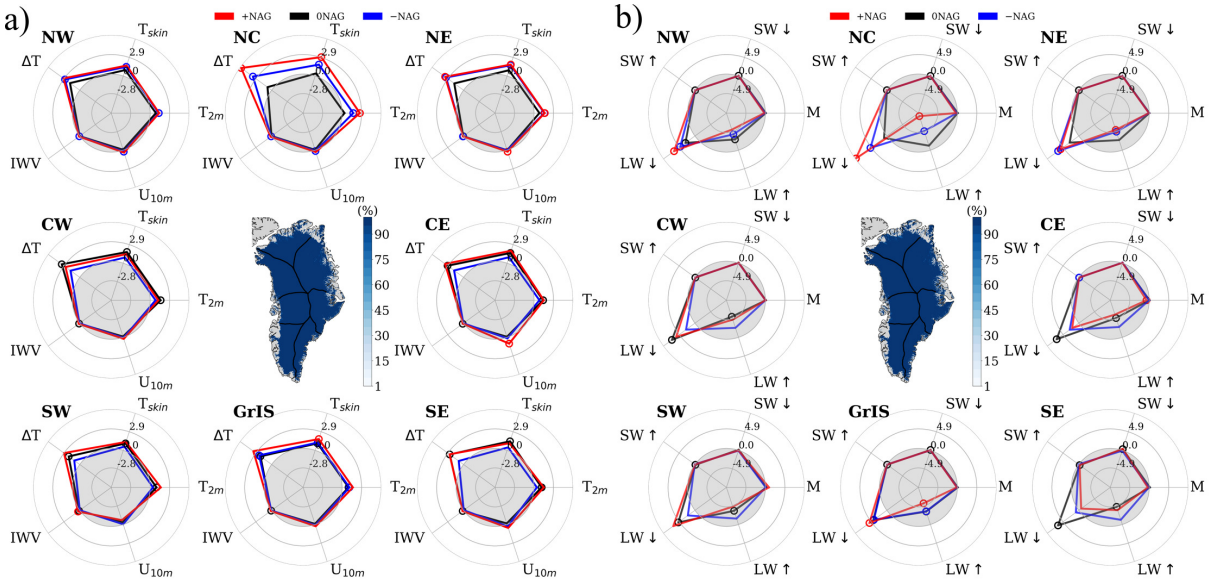

Figure S17. Changes in atmospheric variables influencing SEB components in the winter accumulation zone for each NAG phase. The spatial relative frequency of accumulation is shown at the center. Negative changes are limited by the gray area. Hollow circles indicate significant mean differences based on the Wilcoxon rank-sum statistic test for unpaired sets with a confidence higher than 90%.